

Formation of large-area GaN nanostructures with controlled geometry and morphology using top-down fabrication scheme

Dipak Paramanik

Material Measurement Laboratory, National Institute of Standards and Technology, Gaithersburg, Maryland 20899

Abhishek Motayed^{a)}

Material Measurement Laboratory, National Institute of Standards and Technology, Gaithersburg, Maryland 20899 and Institute for Research in Electronics and Applied Physics, University of Maryland, College Park, Maryland 20742

Geetha S. Aluri

Material Measurement Laboratory, National Institute of Standards and Technology, Gaithersburg, Maryland 20899

Jong-Yoon Ha and Sergiy Krylyuk

Material Measurement Laboratory, National Institute of Standards and Technology, Gaithersburg, Maryland 20899 and Institute for Research in Electronics and Applied Physics, University of Maryland, College Park, Maryland 20742

Albert V. Davydov

Material Measurement Laboratory, National Institute of Standards and Technology, Gaithersburg, Maryland 20899

Matthew King, Sean McLaughlin, Shalini Gupta, and Harlan Cramer

Northrop Grumman ES, Linthicum, Maryland 21090

(Received 27 April 2012; accepted 3 July 2012; published 26 July 2012)

This paper details the fabrication of GaN nanoscale structures using deep ultraviolet lithography and inductively coupled plasma (ICP) etching techniques. The authors controlled the geometry (dimensions and shape) and surface morphology of such nanoscale structures through selection of etching parameters. The authors compared seven different chlorine-based etch chemistries: Cl₂, Ar, Cl₂/N₂, Cl₂/Ar, Cl₂/N₂/Ar, Cl₂/H₂/Ar, and Cl₂/He/Ar. The authors found that nitrogen plays a significant role in fabricating high quality etched GaN nanostructures. This paper presents the effects of varying the etch parameters, including gas chemistry, gas flow rate, ICP power, rf power, chamber pressure, and substrate temperature, on the etch characteristics, including etch rate, sidewall angle, anisotropy, mask erosion, and surface roughness. Dominant etch mechanisms in relation to the observed characteristics of the etched features are discussed. Utilizing such methods, the authors demonstrated the fabrication of nanoscale structures with designed shapes and dimensions over large area. Nanocolumns with diameter of 120 nm and height of 1.6 μm with sidewall angle of 86° (90° represent a vertical sidewall) were fabricated. Nanocones with tip diameter of 30 nm and height of 1.6 μm with sidewall angle of 70° were demonstrated. Such structures could potentially be used in light-emitting diodes, laser diodes, photodetectors, vertical transistors, field emitters, and photovoltaic devices. This study indicates the feasibility of top-down methods in the fabrication of next-generation nitride-based nanoscale devices, with large-area uniformity and scalability. © 2012 American Vacuum Society. [<http://dx.doi.org/10.1116/1.4739424>]

I. INTRODUCTION

Recently, GaN-based nanoscale structures have gained tremendous research interest. A of device structures and applications have been demonstrated using such nanostructures.¹⁻⁴ Significant advances have been made in the growth methods of GaN 3D nanoscale structures, including large-area fabrication and vertically aligned core-shell structures.⁵⁻⁷ However, bottom-up growth methods, despite resulting in superior performance, still lack control over the dimensions, orientation, separation, and dopant

incorporation.⁸ Bottom-up techniques face significant challenges in scaling-up over large areas, which is essential for successful device implementations.

We may resolve such difficulties utilizing standard micro- and nanofabrication methods to develop such nanoscale structures. As the dimensions are defined by such highly mature technologies as lithography and etching, and dopant profiles are established during the growth of thin films, these methods promise reproducible large-area fabrication of regular array nanostructures with controlled geometry for device applications. However, top-down methods also face significant challenges for controlling: (1) surface morphology, (2) structure anisotropy, (3) nanoscale high-aspect ratio (HAR) structures, and (4) subsurface damage. For GaN, the

^{a)} Author to whom correspondence should be addressed; electronic mail: amotayed@nist.gov

subsurface damage is perhaps the most crucial factor for determining the feasibility of these methods, since plasma etching is the only effective way to etch such 3D structures in GaN. When designing an etch process to produce nanoscale structures, we have to find a suitable trade-off between certain parameters, such as acceptable etch rate, anisotropy, and subsurface damage.

Significant advances have been made in plasma etching of GaN in the last decade. Early reports on inductively coupled plasma (ICP) etching of GaN were made by Shul *et al.*,⁹ where they indicated GaN etch rate in excess of $0.5 \mu\text{m}/\text{min}$ using $\text{Cl}_2/\text{H}_2/\text{Ar}$ chemistry. Smith *et al.*¹⁰ reported a maximum etch rate of $980 \text{ nm}/\text{min}$ with an etch chemistry of Cl_2/Ar . The breaking of Ga–N bonds by ion bombardment was speculated to be the rate-limiting step in ICP etching of nitrides. Shul *et al.*¹¹ reported $\text{Cl}_2/\text{N}_2/\text{Ar}$ chemistry among other plasma chemistries, where the addition of nitrogen was linked to the reduction of nitride etch rates. They indicated that under the experimental plasma condition, the etch was dominated by ion bombardment. Sheu *et al.*¹² compared the etching rates of Cl_2/N_2 and Cl_2/Ar chemistries, and the higher etch rate for Cl_2/Ar recipe was attributed to the more efficient dissociation of Cl_2 by Ar ions. Kim *et al.*¹³ studied the relative amounts of positive ion species and neutral species in Cl_2/BCl_3 plasma in an ICP reactor using plasma mass spectrometry. It was shown that ion-assisted chemical desorption was enhanced with the addition of BCl_3 to Cl_2 . Hahn *et al.*¹⁴ studied the effects of adding He, Ar, and Xe to Cl_2 in ICP plasma and showed that the etch rate was highest for the Cl_2/He . Lee *et al.*¹⁵ also studied the effects of gas additives such as H_2 , Ar, and CH_4 in Cl_2 -based chemistries for ICP etching of GaN and InGaN. They used rare-gas actinometry to identify the increased concentration of atomic Cl radical when Ar is added to the Cl_2/H_2 , which resulted in higher etch rates as compared to Cl_2/H_2 only. Excellent numerical simulations have been presented by Despiau-Pujo *et al.*,¹⁶ who used a two-dimensional fluid model to simulate the ion and radical fluxes in Cl_2/Ar plasma in an ICP reactor with varying process parameters and used the simulation results to explain observed experimental etching of GaN. Although the above-mentioned works provide significant relevant information on ICP etching of nitrides, they mostly focus on producing micrometer scale features. The most important difference between etching a micrometer scale feature and a nanoscale feature is the thickness of the etch mask that can be used, i.e., for smaller features thinner etch mask is needed. As physical sputtering is inevitably present in most ICP processes, thinner etch masks make it difficult to produce HAR nanoscale structures.

In recent years, there have been few reports on nitride nanostructures formed by etching. Rong *et al.*¹⁷ investigated Cl_2 -based ICP etching of GaN by Ar, Cl_2 , and N_2 gas mixtures for developing high-aspect ratio nanophotonic crystal waveguides in GaN. They demonstrated the beneficial role of N_2 in producing anisotropic smooth etch profiles, with reduction in trenching at the bottom of etched holes. Also, GaN/AlGaIn one-dimensional photonic crystals were demonstrated by Stomeo *et al.*¹⁸ using $\text{N}_2/\text{Ar}/\text{SiCl}_4$ plasma. However, more detailed and comprehensive study of the effects

of various etching parameters on the quality of the etch for the nanoscale HAR structures is required. Such study should address specific questions, such as how to have acceptable etch rate and anisotropy with minimum surface damage, or the maximum etch depth possible without significant mask erosion. Also, microloading effects are significant for HAR nanostructures, which should be investigated in detail. In addition, for various device applications, such as light-emitting diodes, laser diodes, photodetectors, vertical transistors, field emitters, and photovoltaic devices, production of features with various shapes such as rods, cones, and needles with nanoscale dimensions is needed. Motivation for the current work is to identify top-down fabrication methods for producing GaN nanoscale structures with designed shapes, dimensions, and morphology suitable for device applications.

In this paper we discuss our work on developing GaN nanoscale structures using deep-ultraviolet lithography (deep-UV) and ICP etching. Our goal was to understand the effects of various etch conditions on the feature geometry and final morphology, and to produce features with controlled shapes by properly designing the etch process. We compared seven different etch chemistries— Cl_2 , Ar, Cl_2/N_2 , Cl_2/Ar , $\text{Cl}_2/\text{N}_2/\text{Ar}$, $\text{Cl}_2/\text{H}_2/\text{Ar}$, and $\text{Cl}_2/\text{He}/\text{Ar}$. We present detailed results for varying individual etch parameters, including gas chemistry, gas flow rate, ICP power, rf power, chamber pressure, and substrate temperature. A figure of merit was proposed to quantitatively characterize the effects of these parameters on the quality of etched structures.

II. EXPERIMENT

The GaN samples used for this study were grown on *n*-type Si (111) substrates with sheet resistance of $15 \text{ k}\Omega/\text{sq}$. A commercial metalorganic chemical vapor deposition system was used to grow the GaN epitaxial layers. The thickness of the GaN epilayer was in the range from 0.8 to $1.5 \mu\text{m}$. Intermediate $\text{Al}_{1-x}\text{Ga}_x\text{N}$ buffer layers with varying x and thickness ranging from 125 to 500 nm were utilized.

After the growth, the wafers were patterned using deep-UV lithography. The lithography mask used for this study had different patterns (square, circle, hexagon, octagon, five-pointed star, seven-pointed star, and diamond) with diameters from 10 to 250 nm and pitches ranging from $20 \mu\text{m}$ to 100 nm . The etch mask used for this study was Ti/Ni ($50 \text{ nm}/120 \text{ nm}$) deposited by electron-beam evaporation and patterned by lift-off.

For the etching experiments, the wafers were diced into $20 \text{ mm} \times 20 \text{ mm}$ pieces and mounted on a 4 in. Si carrier wafer with 50 nm atomic layer deposited Al_2O_3 . Thermal contact to the carrier wafer was made with suitable thermal grease. When the same etching conditions are applied to a full 4 in. GaN wafer it is a possibility that macroloading effects can locally alter the etching characteristics. However, we conducted experiments both on pieces and large wafers and did not observe any significant macroloading effects. The samples were etched in an Oxford PlasmaLab 100 ICP system with an Oxford remote ICP380 source. The helium pressure for wafer

back-side cooling was 1.33 kPa (10 Torr). For every etch process the dc self-bias was recorded. Before every etch experiment, the ICP chamber was cleaned and conditioned.

After the ICP etching, the samples were put in HF:HNO₃:H₂O (1:1:10) solution for 2 min to remove the etch mask and clean both etch debris and redeposit. The samples were then observed with a 70° tilted sample-holder in a field-emission scanning electron microscope (FESEM). In order to compare results for the different etch conditions, we computed the etch rate and sidewall angle, θ , for every sample.

III. RESULTS AND DISCUSSION

A schematic of an ideal etch profile with a perfect 90° sidewall angle is shown in Fig. 1(a). This represents an ideal anisotropic etch with infinite selectivity, i.e., the etch rate of the mask material is negligible compared to the etch rate of the substrate material. However, in any given plasma etch process, there is always a certain degree of lateral etch, which produces tapered structures with diameters smaller than the starting etch mask pattern, as shown in Fig. 1(b). The two most significant sources of lateral etch are mask erosion and wider ion angular distribution function (IADF).¹⁹ The IADF represents the spread of the angular distribution of the ions impinging on the surface. Ions, while crossing the sheath, encounter collisions with gas molecules, which broadens their IADF. Smaller full width at half maximum of the IADF results in higher anisotropy of the etched structure.

For quantitative comparison of the quality of the etch for various etching conditions, we proposed a figure of merit (FOM) defined as

$$\text{FOM} = \frac{h}{d_i} \times \frac{d_f}{d_i} \times \frac{\theta}{90^\circ}, \quad (1)$$

where h is the height of the etched structure, d_i is the initial diameter of the etch mask, d_f is the final tip diameter of the

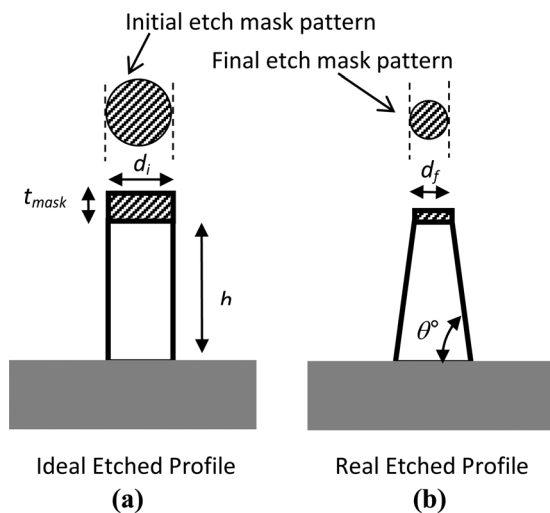


Fig. 1. (a) Schematic representation of an ideal etched structure with infinite mask selectivity, and perfect anisotropy, (b) representation of a real etched feature with tapering and mask erosion.

etch pattern, θ is the sidewall angle, and t_{mask} is the etch mask thickness, as shown in Fig. 1. The proposed FOM can be thought as a modified aspect ratio, with the mask selectivity and anisotropy incorporated.

Although we had various shapes and diameters on the etch mask, for comparative purposes we will present the results for the 850 nm (measured by FESEM) diameter circle as seen in Fig. 2. As the mask pattern was formed by metal lift-off, there is certain degree of edge nonuniformity present on the dots, as can be seen on the inset of Fig. 2. These non-uniformities of the etch mask also get transferred to the sidewalls of the etched patterns.

A. Gas chemistry dependent etching behavior

Figure 3 shows the etch profiles for seven different etch chemistries. The four numbers on each pillar are as follows: (1) diameter at the top of the pillar in nanometers, (2) diameter at the bottom in nanometers, (3) on the left side the total height of the pillar in nanometers, and (4) angle θ of the sidewall measured in degrees at the top left corner of the image. The computed etch rate, FOM, and the measured dc self-bias are summarized in Table I. For this experiment, the ICP power was 800 W, rf power was 300 W, chamber pressure was 0.66 Pa (5 mTorr), and substrate temperature was maintained at 40 °C. The total flow rate for all the chemistries was kept constant at 32 SCCM (SCCM denotes cubic centimeters per minute at standard temperature and pressure). Comparing the FESEM images of the features etched using pure Cl₂ and Ar (the first two images in Fig. 3), certain key aspects of GaN etch mechanisms can be identified. The etch rate is significantly higher in the case of pure Cl₂ compared to pure Ar. This highlights the crucial role of chemical reaction combined with physical sputtering in etching of GaN. In the case of the Cl₂ only process, both Cl neutral radicals, and Cl⁺ and Cl₂⁺ ions are present in the plasma.¹⁶ The Cl radicals promote the chemical etch, whereas the Cl⁺ and Cl₂⁺ ions provide the physical sputtering. In the case of pure Ar plasma, only sputtering due to Ar⁺ ions is present. This is also reflected in the dc self-bias values in Table I: the dc self-bias is 473 V for Ar compared to 594 V for Cl₂ plasma.

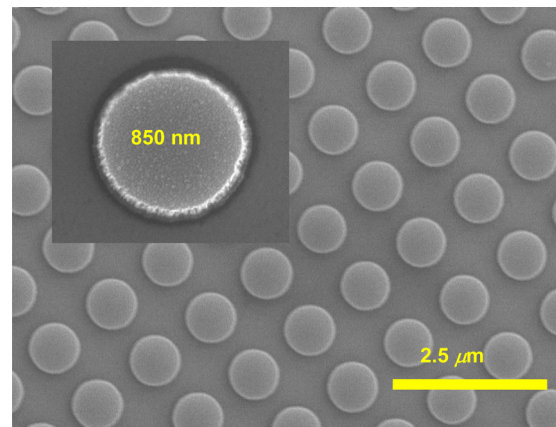


Fig. 2. (Color online) FESEM image of metal dots (850 nm diameter) formed by lift-off technique on GaN. The inset shows a single dot where the edge roughness is visible.

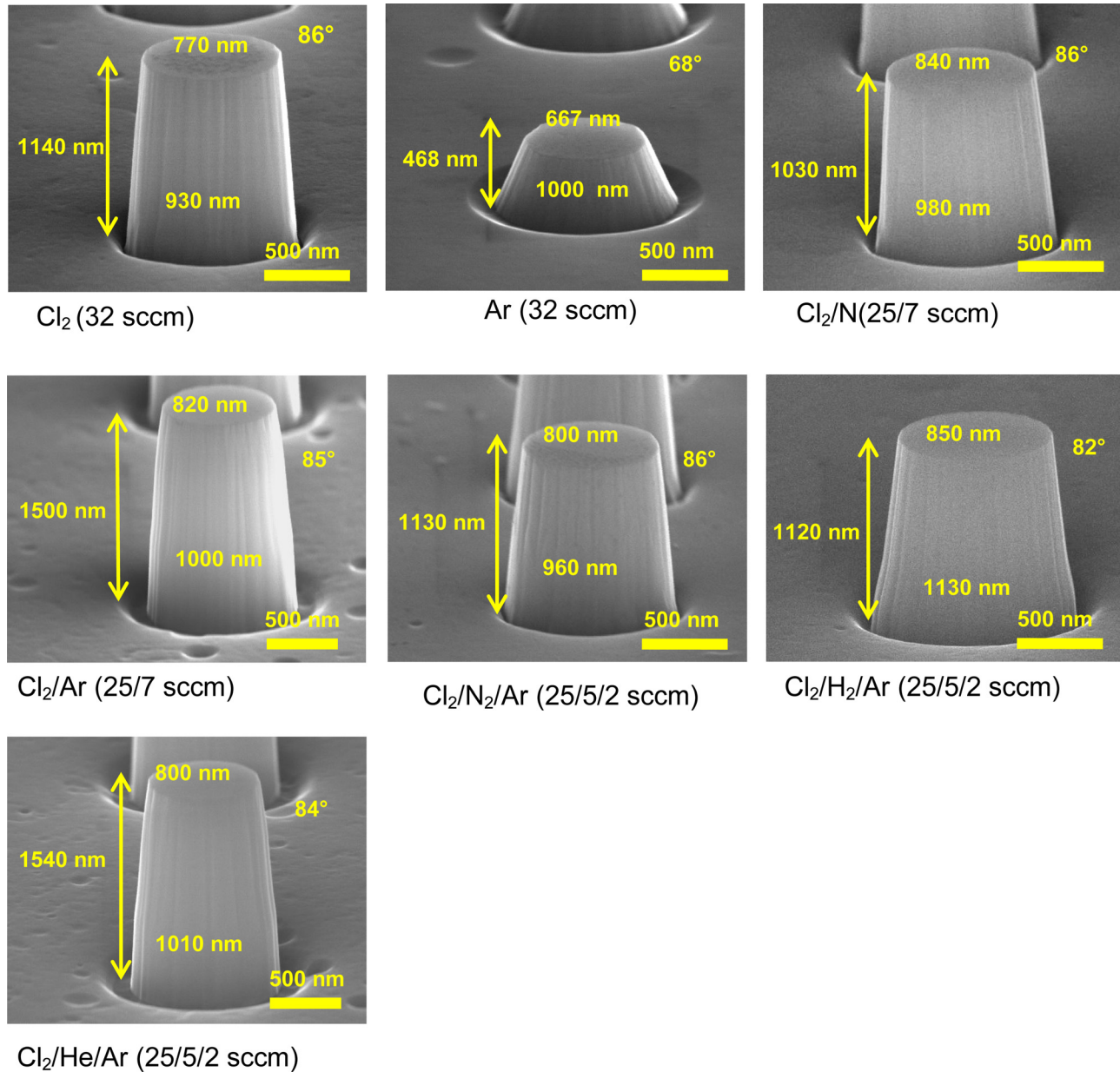


FIG. 3. (Color online) FESEM images of pillars etched using different plasma chemistries. The starting etch pattern was an 850 nm diameter circle. The etch parameters were ICP power 800 W, rf power 300 W, chamber pressure 0.66 Pa, etch time 4 min, and substrate temperature 40 °C. The imaging is done after removal of the etch mask.

The significant difference in the dc self-bias can be understood by considering the following relationship between the rf power P_{rf} , ion flux crossing the sheath F_{ion} , and dc self-bias V_{dc} (Ref. 20):

$$P_{\text{rf}} \propto V_{\text{dc}} F_{\text{ion}}. \quad (2)$$

In the case of Ar only plasma, the ICP source is able to produce more Ar ions, leading to an increase in the ion flux, as compared to the Cl₂ case where both radicals and ions are present. From Eq. (2), we can see that increase in ion flux for constant rf power would lead to a decrease of the dc self-bias. When comparing the final diameter of the etched pillar (667 nm) with the starting diameter of the etch mask (850 nm), it is evident that there is significant mask erosion

in Ar plasma etch, which is expected for pure physical sputtering. Mask erosion is also present in Cl₂ plasma, which could be due to the formation of Ni and Ti chlorides in the presence of highly reactive Cl radicals. Significant trenching at the bottom of the Ar-etched pillar indicates the increased spreading of IADF for Ar plasma as compared to the Cl₂. For the Ar process the deep trenching also results from the scattering of ions impinging on an angled surface.

The addition of 7 SCCM of N₂ or Ar to Cl₂ (keeping the total flow to 32 SCCM) results in significant changes in the etch characteristics. Compared to pure Cl₂, there is etch rate suppression with the addition of N₂ and significant etch rate enhancement with the addition of Ar (see Table I). Etch rate suppression with the addition of N₂ has been observed by Shul *et al.*¹¹ However, Sheu *et al.*¹² reported higher GaN

TABLE I. Etch rates, FOMs, and dc self-bias values for different etch chemistries.

Etch chemistry (SCCM)	Etch rate ($\mu\text{m}/\text{min}$)	FOM	Direct current bias (V)
Cl_2/Ar (25/7)	0.37	1.61	547
$\text{Cl}_2/\text{He}/\text{Ar}$ (25/5/2)	0.38	1.59	548
$\text{Cl}_2/\text{H}_2/\text{Ar}$ (25/5/2)	0.28	1.20	565
$\text{Cl}_2/\text{N}_2/\text{Ar}$ (25/5/2)	0.28	1.20	540
Cl_2 (32)	0.28	1.16	594
Cl_2/N_2 (25/7)	0.25	1.14	567
Ar (32)	0.11	0.33	473

etch rate for the Cl_2/N_2 recipe compared to the Cl_2/Ar recipe, which is opposite of what we have observed. Comparing the dc self-bias in Table I, it is evident that the addition of Ar or N_2 results in the reduction of dc self-bias from pure Cl_2 value, which only indicates an increase in ion flux in both cases. As the mass of N_2^+ ion is less than Ar^+ , the observed difference in etch rate could be due to the difference in sputtering yields. The increase in etch rate due to Ar addition has been attributed to the increase in ion density due to Penning ionization.¹⁵ Also in Fig. 3, suppression of etch mask erosion is observed with the addition of N_2 compared to pure Cl_2 and Cl_2/Ar recipes.

Interesting effects are observed with the addition of two inert gases while keeping the total flow constant at 32 SCCM (see the last three images in Fig. 3). The first observation is the similarity of the $\text{Cl}_2/\text{He}/\text{Ar}$ (25/5/2 SCCM) and Cl_2/Ar (25/7 SCCM) etched features. The dc self-bias values and FOMs are also identical as seen in Table I. The rough sidewall morphology is also quite similar in both cases. Even the trenching at the base of the pillars and the bottom plane morphology appear identical for both the etches. Although the ionization energies are different for Ar and He, both are monoatomic gases, which might be the reason for the observed similarity of their etch characteristics. Although $\text{Cl}_2/\text{N}_2/\text{Ar}$ produces very similar characteristics to Cl_2/N_2 etch, the $\text{Cl}_2/\text{H}_2/\text{Ar}$ process produces a very distinct shape with sloped sidewalls. Suppression of GaN etch rate with the addition of H_2 has been observed for Cl_2/Ar plasma by Shul *et al.*¹¹ This was attributed to the consumption of reactive Cl radical by H forming HCl.

Comparing the FOMs for all seven etches (see Table I), it is clear that although Cl_2/Ar and $\text{Cl}_2/\text{He}/\text{Ar}$ have the highest FOMs, the sidewall morphology is rough for both of them. $\text{Cl}_2/\text{H}_2/\text{Ar}$ etch has an FOM comparable to $\text{Cl}_2/\text{N}_2/\text{Ar}$; however, rough surface morphology is prominent in the $\text{Cl}_2/\text{H}_2/\text{Ar}$. Also, H_2 -based etches are avoided due to the possibility of Mg dopant passivation in *p*-GaN. It is interesting to note that there is no observable mask erosion in the case $\text{Cl}_2/\text{H}_2/\text{Ar}$. Considering the overall performances, we decided to further study the $\text{Cl}_2/\text{N}_2/\text{Ar}$ chemistry, which provides a reasonable etch rate and FOM.

B. Effect of gas flow on the etch characteristics

We varied the total gas flow rate for the $\text{Cl}_2/\text{N}_2/\text{Ar}$ chemistry with the constant constituent ratio (25:5:2). By varying

the flow rate, while keeping the pressure constant, we can observe the effect of gas residence time on the etch characteristics. Also, by increasing the total flow rate, we can identify whether the etch is reactant limited or not. For this experiment, the ICP power was 800 W, rf power was 300 W, chamber pressure was 0.66 Pa (5 mTorr), and the substrate temperature was maintained at 40 °C. Looking at Fig. 4, it is clear that the total gas flow rate has only a modest effect on the etch characteristics. This is consistent with the graph presented in Fig. 5, where the dc self-bias is shown to be constant with flow rate. According to Eq. (2), this indicates that the total ion flux is independent of the gas flow rate. Khan *et al.*²¹ also observed very little change in GaN etch rate with increasing flow rates for 70% Cl_2 in Cl_2/Ar etch. The most interesting point is the slight decrease of the etch rate with increasing gas flow rate. Keeping the pressure constant while increasing the flow rate decreases the residence time of reactive radical and ions in the chamber. Thus, the chemical species do not have sufficient time to support etching. As expected, the sidewall profiles and bottom plane morphologies are quite similar for all the flow rates, except at the highest flow rate. Rough sidewall morphology for 48 SCCM total flow rate indicates inefficient removal of the etch products. One interesting point evident from Fig. 4 is that the mask erosion is significantly suppressed at higher flow rates, the reason for which is not clear at this point.

C. Effect of ICP power on the etch characteristics

One of the most significant etch parameters is the ICP power. Increasing ICP power results in higher density of ions and radicals in the plasma. This, in general, increases the chemical component of the etch. We varied the ICP power from 500 to 1500 W for the $\text{Cl}_2/\text{N}_2/\text{Ar}$ chemistry while keeping the rf power constant at 300 W. The FESEM images in Fig. 6 show the pillars etched at different ICP power levels. It is clear from Figs. 6 and 7 that ICP power level has significant influence on the etch characteristics and dc self-bias values. Table II indicates the improvement of FOM for higher ICP power level. It is worth mentioning that the proposed FOM gives equal weight to every profile parameter. In applications where a single parameter (e.g., height or diameter) has higher significance, the FOM can be modified with an appropriate multiplier, which would enable comparison between two etch processes.

From Fig. 6 the increase in the etch rate with increasing ICP power is evident. Smith *et al.*¹⁰ observed a similar increase in the etch rate of GaN, which was attributed to the increase in Cl radical and ion density. In their work the increase was slowed down after 800 W. However, Sheu *et al.*¹² reported an initial increase of etch rate of GaN in Cl_2/Ar plasma up to 600 W of ICP power followed by a decrease in the etch rate. The dc self-bias was observed to decrease with increasing ICP power. The increase of etch rate was attributed to the fact that etch was reaction limited. Hahn *et al.*¹⁴ also observed a similar increase followed by a decrease in the etch rate with increasing ICP power. The initial increase was again attributed to the reaction-limited

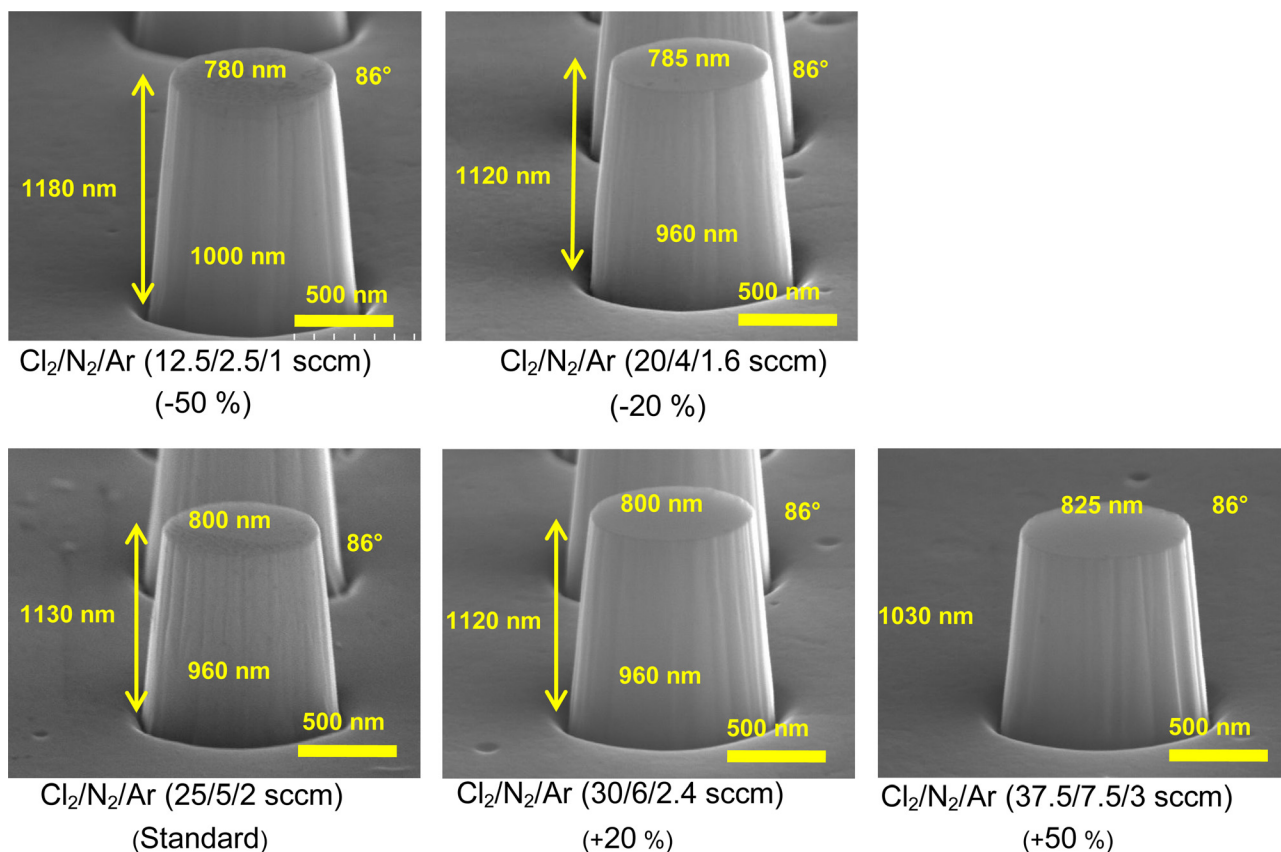


Fig. 4. (Color online) FESEM images of pillars etched using different flow rates for $\text{Cl}_2/\text{N}_2/\text{Ar}$ chemistry with a constant (25:5:2) constituent ratio. The starting etch pattern was 850 nm diameter circle. The etch parameters were ICP power 800 W, rf power 300 W, chamber pressure 0.66 Pa, etch time 4 min, and substrate temperature 40 °C. The imaging is done after removal of the etch mask.

regime, whereas the decrease was attributed to lower ion energies due to the reduction in dc self-bias and ion-assisted desorption of reactive species at the substrate prior to the etch reactions.

Despiau-Pujo *et al.*¹⁶ and Tinck *et al.*²² showed through simulation that ion fluxes increase with increase in ICP power. Ion flux (F_{ion}) in a collisionless sheath is given by the following relationship¹⁶:

$$F_{\text{ion}} = n_{\text{ion}} \sqrt{\frac{qT_e}{m_{\text{ion}}}}, \quad (3)$$

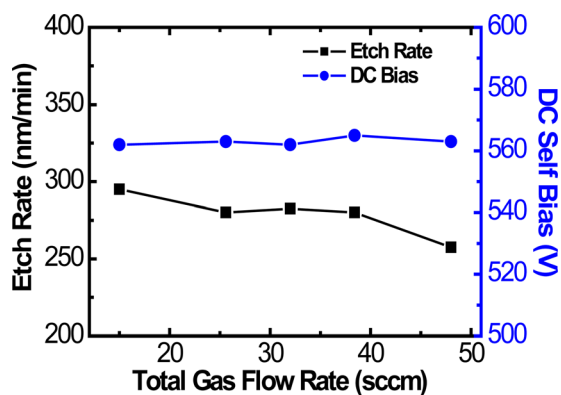


Fig. 5. (Color online) Etch rates and dc self-bias values as a function of total gas flow rate in SCCM for the $\text{Cl}_2/\text{N}_2/\text{Ar}$ chemistry.

where n_{ion} is the ion density at the edge of the sheath, T_e the electron temperature, q is the electron charge, and m_{ion} is the ion mass. From Eq. (3), it is clear that the ion-flux increase at higher ICP power levels is due to the increased electron temperature. Both Tinck *et al.*²² and Despiau-Pujo *et al.*¹⁶ noted in their simulation a substantial increase in all ion fluxes with source power, while Cl radical flux, which is always orders of magnitude higher than the ion fluxes, remained fairly constant. Based on such simulation results, it is reasonable to argue that the increase in the etch rate due to the increase in the ICP power (as seen in Fig. 7) is due to the increase in ion fluxes rather than radical fluxes. The increase in ion fluxes is also evident from the graph of etch rate and dc self-bias versus ICP power presented in Fig. 7, where a decrease in dc bias is observed with increasing ICP power. According to Eq. (2) an increase in ion flux for a constant rf power leads to a decrease in the dc self-bias. Due to enhanced physical sputtering resulting from increased ion bombardment, there is significant mask erosion at higher ICP power levels. It is known that at higher ICP power levels the etch is physical sputtering dominated; hence not chemically selective.²³ Also, due to the decrease in dc self-bias with increasing ICP power, the IADF becomes wider, resulting in more isotropic etch. This would explain the increased tapering and decrease in the sidewall angle for 1500 W ICP power. For 1500 W ICP power, we have completely etched the GaN, and the Si substrate is visible. The bottom plane

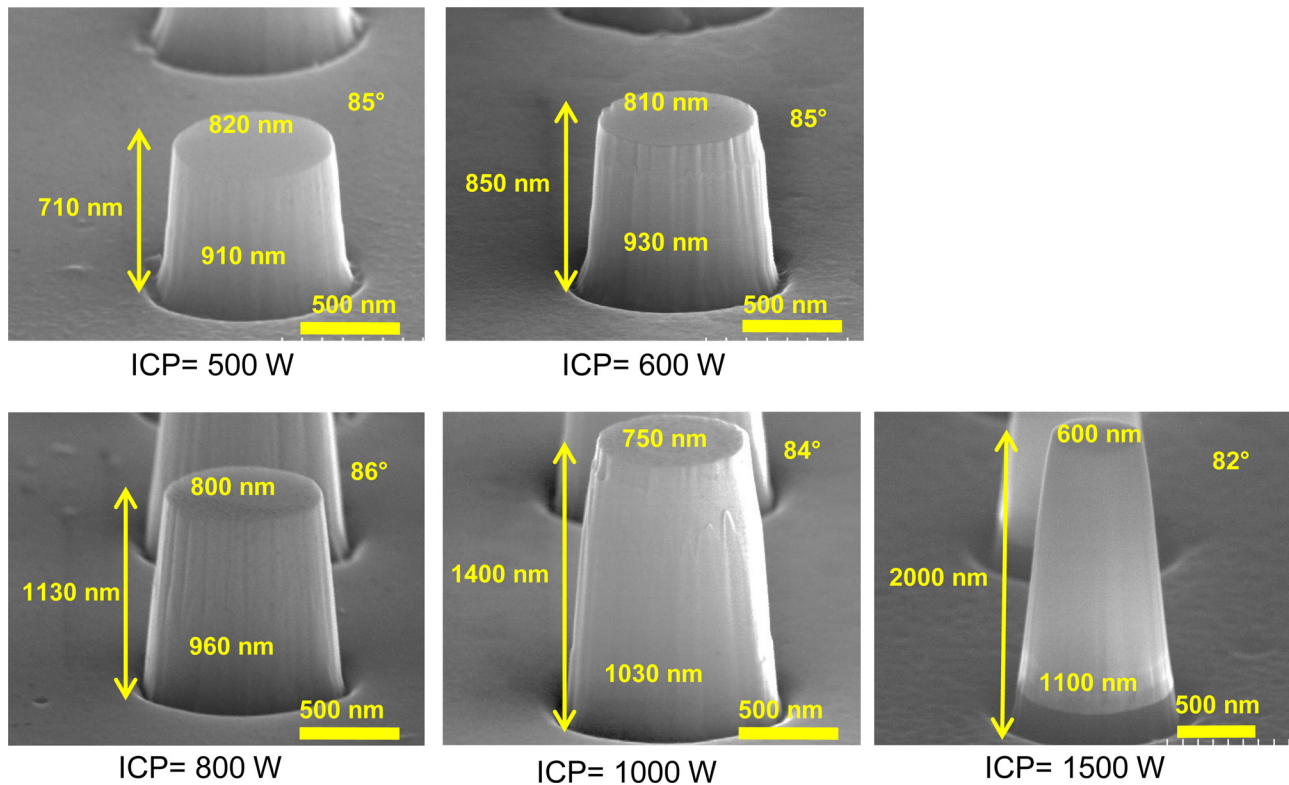


Fig. 6. (Color online) FESEM images of pillars etched using different ICP powers for $\text{Cl}_2/\text{N}_2/\text{Ar}$ (25/5/2 SCCM) chemistry. The starting etch pattern was 850 nm diameter circle. The etch parameters were rf power 300 W, etch time 4 min, chamber pressure 0.66 Pa, and substrate temperature 40 °C. The imaging is done after removal of the etch mask.

morphology did not show any dependence on the ICP power levels. It is interesting to note that the sidewalls are smoother for higher ICP levels compared to lower ICP levels (see Fig. 6). This is possibly due to efficient sputter desorption of the etch products and redeposits.

D. Effect of reactive ion etching power on the etch characteristics

Another significant etch parameter is the rf power applied to the cathode. The rf power directly affects the sheath thickness and the dc self-bias; hence the mean ion energy.²⁴ In other words, the rf power modifies the ion energy distribution function (IEDF). As IEDF directly controls ion

bombardment, physical sputtering increases with increasing rf power. It is worth pointing out that the ion and neutral radical densities are unaffected by the rf power change in an ICP reactor. It is clear from Fig. 8 that the etch rate is significantly affected by the increase in rf power, as compared to the changes in the ICP power. Significant mask erosion is also prominent for higher rf power levels. The dc self-bias increases with the increase in rf power, as can be seen in Fig. 9. This is a common observation in ICP etching and is consistent with Eq. (2). The dc self-bias increases in response to an increase in the rf power, as the ion flux remains constant for constant ICP power levels.

Sheu *et al.*¹² noted the existence of a threshold energy in terms of rf power level (i.e., significant etch rate enhancement beyond 200 W of rf power), for ICP etching of GaN using Cl_2/Ar chemistry. It was suggested that the Ga–N bond breaking by ion bombardment may be the rate-limiting step. However, for Cl_2/N_2 chemistry, no such threshold energy

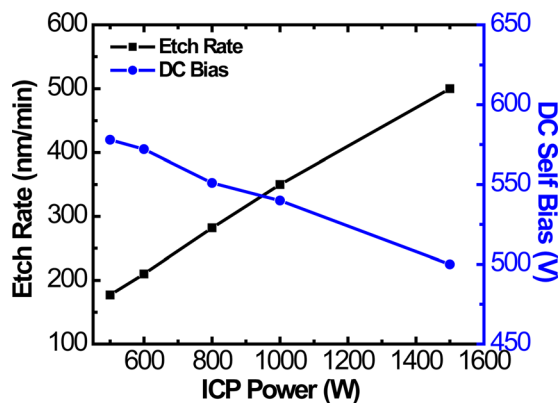


Fig. 7. (Color online) Etch rates and dc self-bias values as a function of ICP power for the $\text{Cl}_2/\text{N}_2/\text{Ar}$ chemistry.

TABLE II. FOMs for different ICP powers computed from Fig. 6 using Eq. (1).

ICP power (W)	FOM
500	0.76
600	0.90
800	1.20
1000	1.36
1500	1.51

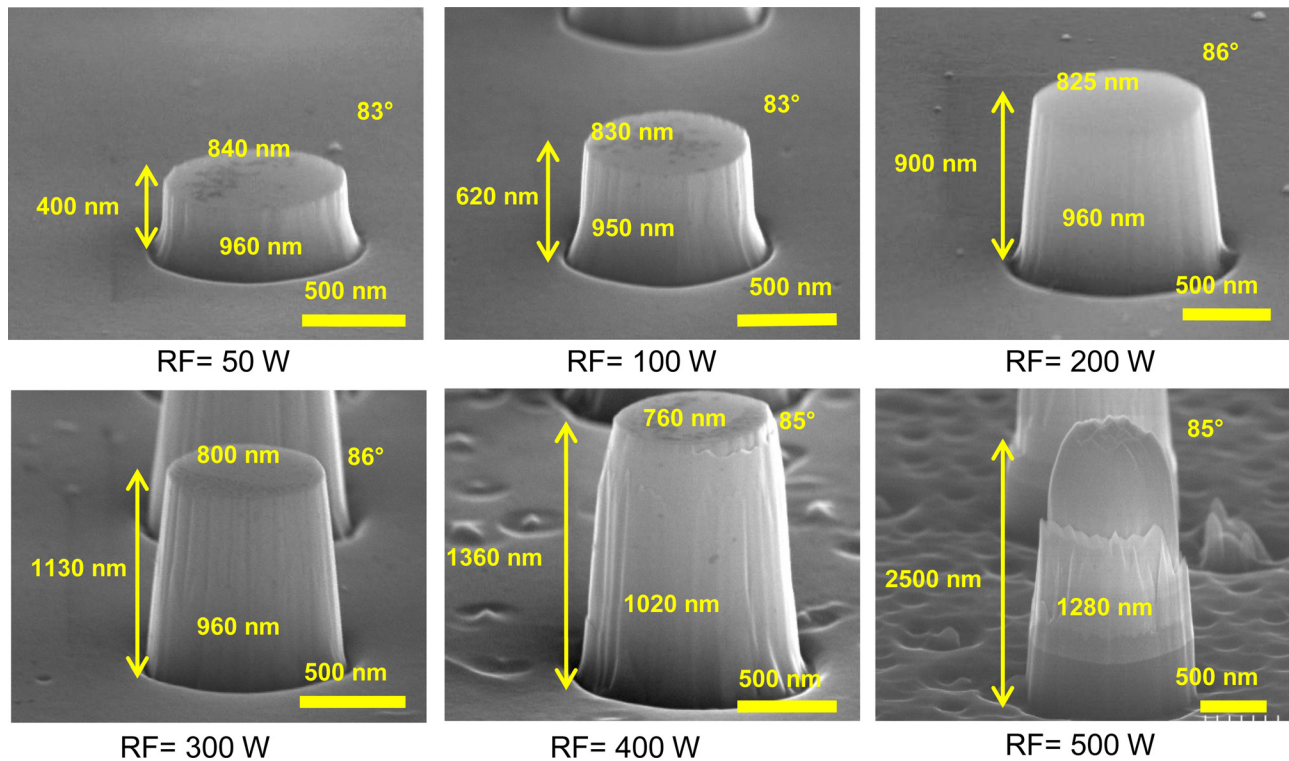


Fig. 8. (Color online) FESEM images of pillars etched using different rf power applied to the cathode for $\text{Cl}_2/\text{N}_2/\text{Ar}$ (25/5/2 SCCM) chemistry. The starting etch pattern was 850 nm diameter circle. The etch parameters were ICP power 800 W, chamber pressure 0.66 Pa, etch time 4 min, and substrate temperature 40 °C. The imaging is done after removal of the etch mask.

was observed. In our case, for the $\text{Cl}_2/\text{N}_2/\text{Ar}$ recipe we also did not observe an activation barrier to the etching of GaN as function of rf power at ICP power of 800 W. The observed etch rate increase (Fig. 9) with increase in rf power is due to the increased sputtering yield for higher ion energies and enhanced desorption of the etch products. Another obvious observation is the increase in sidewall angle for higher rf power levels (as reflected in FOMs in Table III). This suggests smaller FWHM of the IADF at higher rf power levels. However, comparing etching characteristics for rf power of 300 and 500 W, it is clear that there is trade-off between tighter IADF and increase in physical sputtering at higher rf power. The sidewalls start to deteriorate due to sputtering of the etch mask. At 500 W of rf power, there is complete

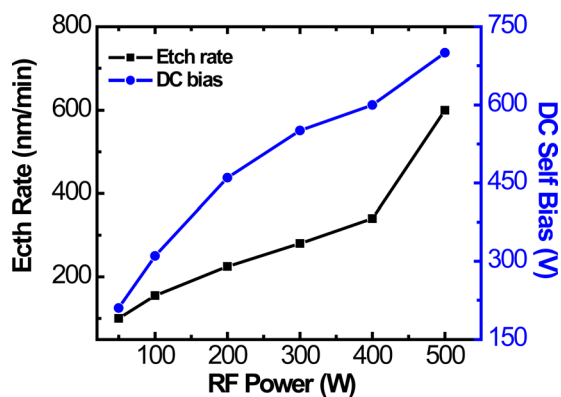


Fig. 9. (Color online) Etch rates and dc self-bias values as a function of rf power for the $\text{Cl}_2/\text{N}_2/\text{Ar}$ chemistry.

removal of the etch mask. The bottom plane morphology becomes rough for rf power of 400 W and higher.

E. Effect of chamber pressure

We varied the chamber pressure from 0.26 Pa (2 mTorr) to 1.99 Pa (15 mTorr), while keeping the ICP power at 800 W, rf power at 300 W, and substrate temperature at 40 °C for the $\text{Cl}_2/\text{N}_2/\text{Ar}$ (25/5/2 SCCM) recipe. Figure 10 presents the etch characteristics as a function of the chamber pressure. From Fig. 11, it is clear that the etch rate and the dc bias decrease with increasing chamber pressure. However, the sidewall morphology and angle show less dependence on pressure.

It is often observed that at lower pressures GaN etch rate increases with increase in process pressure, then saturating and eventually decreasing with pressure.^{9,12,13,25} Initial increase in the etch rate was attributed to the increase in radical concentration with increasing pressure. However, at higher pressure the decrease was attributed to the reduction

TABLE III. FOMs for different rf powers computed from Fig. 8 using Eq. (1).

Radio frequency power (W)	FOM
50	0.43
100	0.66
200	0.98
300	1.20
400	1.35
500	N/A

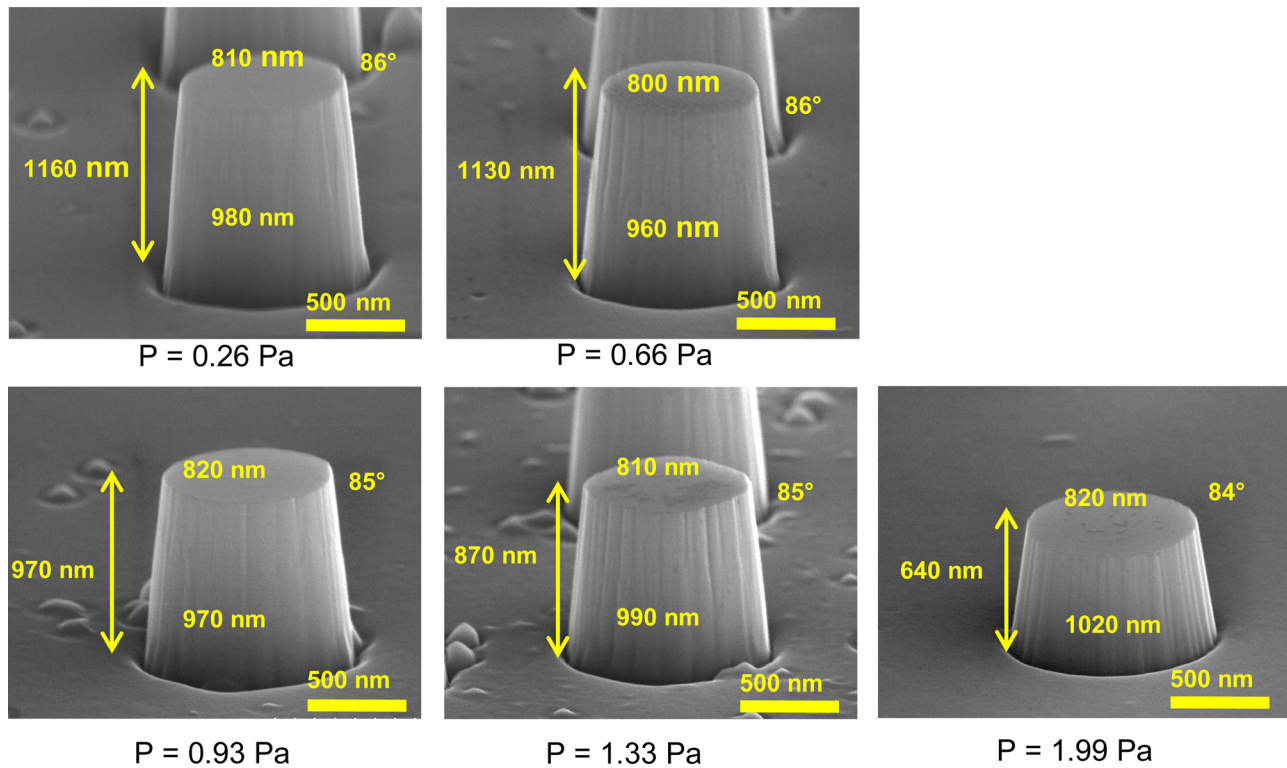


FIG. 10. (Color online) FESEM images of pillars etched using different chamber pressure for $\text{Cl}_2/\text{N}_2/\text{Ar}$ (25/5/2 SCCM) chemistry. The starting etch pattern was 850 nm diameter circle. The etch parameters were ICP power 800 W, rf power 300 W, etch time 4 min, and substrate temperature 40 °C. The imaging is done after removal of the etch mask.

in the ion flux and redeposition of etch products. A decrease in dc bias is noted with increasing pressure. Kim *et al.*¹³ using a quadrupole mass spectrometer observed that the Cl_2^+ and Cl^+ ion densities decrease with increasing pressure for pure Cl_2 plasma. Khan *et al.*²¹ noted that with increasing pressure, the collision frequency of ions that produce neutrals increases, resulting in a decrease in the GaN etch rate.

However, our observed trend of etch rate variation with pressure is different from the other reports. From Fig. 11, it is evident that with increasing pressure, the ion flux increases, resulting in a decrease in the dc bias. Zhimov *et al.*²⁶ noted a similar exception in terms of etch rate and dc bias with increasing pressure. The decrease in the dc bias and etch rate with increase in pressure was attributed to the

remote location of the ICP source in the Oxford PlasmaLab etcher they were using. As described before, the system used for this study also had a remote plasma source.

In our case, the decrease in etch rate with pressure might be attributed to loss of ion energy due to collision in the sheath region. The increase in ion flux with increasing pressure (as indicated by a decrease in dc bias with increasing pressure) is due to impact ionization resulting from collisions in the sheath region. For the dc bias value and other plasma parameters used in our process, we speculate that the collisional ionization dominates over recombination. However, due to the decrease in dc bias and increased collision in the sheath, the mean energy of the ions is smaller at higher pressures. In other words, although at higher pressures there are more ions, the mean energy of the ions bombarding the substrate is lower, together resulting in lower etch rate. Moreover IADF is also broad, resulting in poor anisotropy as evident from Fig. 10 and Table IV.

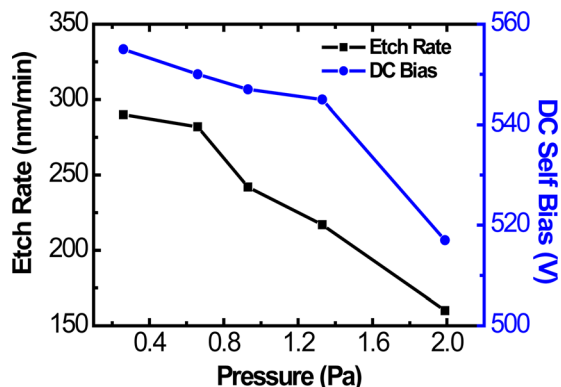


FIG. 11. (Color online) Etch rates and dc self-bias values as a function of the chamber pressure for the $\text{Cl}_2/\text{N}_2/\text{Ar}$ chemistry.

F. Effect of cathode temperature on the etch characteristics

We studied the effect of the cathode temperature on the etch characteristics of GaN for the $\text{Cl}_2/\text{N}_2/\text{Ar}$ chemistry. The other etch parameters were kept constant. Although the samples were mounted on an Si carrier wafer, it is expected that the sample will reach thermal equilibrium with the cathode due to the long wait time between loading and actual etch. The effect of the substrate temperature on the etch characteristics reveals the underlying mechanism of GaN etch.²⁷ Temperature dependence of the etch rate in Fig. 12 is not

TABLE IV. FOMs for different pressure computed from Fig. 10 using Eq. (1).

Pressure (Pa)	FOM
0.26	1.24
0.66	1.20
0.93	1.04
1.33	0.92
1.99	0.68

surprising considering the fact that GaN does not etch spontaneously (Table V). The measured etch rate can be fitted to the activation energy model (Arrhenius plot is shown in Fig. 13),²⁸ where etch rate, $R(T)$, at a particular temperature is given as¹⁹

$$R(T) = R(\text{sat}) \exp(-E_a/k_B T). \quad (4)$$

In Eq. (4), $R(\text{sat})$ is the saturation etch rate at high temperature, E_a is the activation energy, and k_B is the Boltzmann constant. The activation energy from the fit as shown in Fig. 13 is 1.4 meV. The fact that the activation energy is below the thermal energy at -120°C ($k_B T = 13 \text{ meV}$ at -120°C) indicates that ion bombardment is an essential part of GaN etching. Sloped sidewalls at lower temperatures indicate a sputter-dominated regime with limited volatility of etch products. At lower cathode temperatures, the etch product (GaCl_3) might be solid, as the melting point is 77.9°C at atmospheric pressure.

TABLE V. FOMs for different substrate temperatures computed from Fig. 12 using Eq. (2).

Platen temperature ($^\circ\text{C}$)	FOM
200	1.28
120	1.28
40	1.20
0	1.07
-40	1.00
-120	0.91

The dc bias remains constant with the cathode temperature (Fig. 14), which indicates fairly constant ion and radical conditions on the wafer surface. The extent of mask erosion with temperature is surprising. At this point it is not clear why mask erosion is prominent at lower temperatures. Also, it is interesting to note the sidewall roughness increases with increasing temperatures. This may be due to the fact that at lower temperatures the by-product, not being able to evaporate, forms an inhibitor layer. Also, the slight concave profile at high temperatures (120 and 200°C) may be due to high chemical activity of neutral radicals, resembling the undercut in a wet chemical etch.

G. Shape control of GaN nanostructures using etch conditions

In order for top-down fabrication techniques to be applicable for producing the next-generation of GaN nanoscale

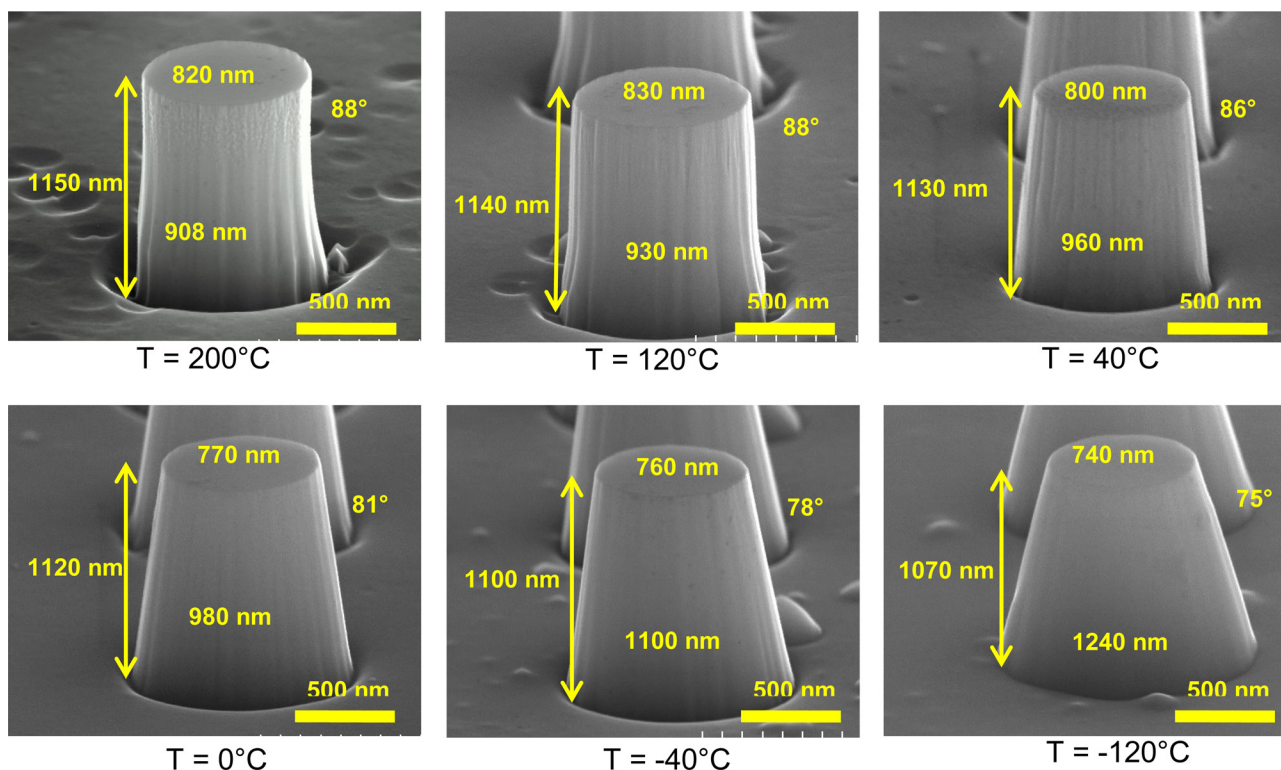


Fig. 12. (Color online) FESEM images of pillars etched at different substrate temperatures for $\text{Cl}_2/\text{N}_2/\text{Ar}$ (25/5/2 SCCM) chemistry. The starting etch pattern was 850 nm diameter circle. The etch parameters were ICP power 800 W, rf power 300 W, chamber pressure 0.66 Pa, and etch time 4 min. The imaging is done after removal of the etch mask.

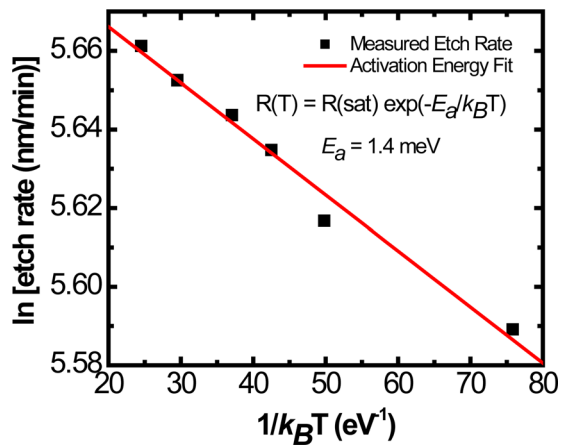


FIG. 13. (Color online) Arrhenius plot of etch rate as a function of the substrate temperature. The activation energy estimate from the linear fit is 1.4 meV.

devices, four basic requirements have to be met: (1) control over dimensions, (2) smooth surfaces (both sidewalls and bottom plane), (3) ability to tailor profiles for specific applications, and (4) large-area uniformity and scalability. Development of GaN nanostructures with HARs (10 and higher) where the diameters are in the range of 150–250 nm require careful design of the etch process and selection of mask material. Sidewall morphology is particularly important when the etched sidewalls are used for regrowth, as in the case of vertical core-shell structures. Also, an unoptimized etching process can result in rough bottom surface morphologies with pits and/or pillars.²⁷ In the case of vertical transistors and light-emitting diodes, a straight profile with 90° angle is highly desirable, whereas for field emitters a sloped profile with sharp tip is needed. The major emphasis of this paper is to demonstrate the top-down fabrication method as a viable alternative for bottom-up growth of GaN nanoscale structures. To demonstrate the point, we fabricated nanostructures of various shapes and dimensions by carefully designing the etch process.

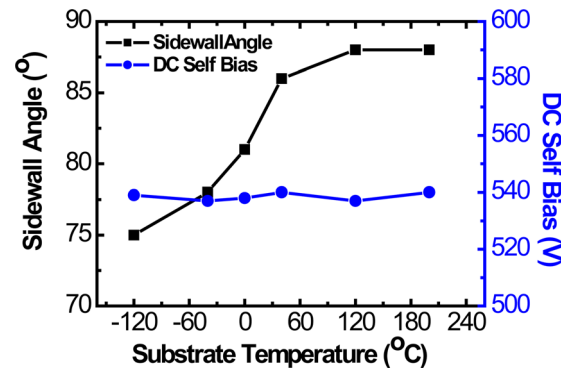


FIG. 14. (Color online) Sidewall angle and dc self-bias values as a function of the substrate temperature for the $\text{Cl}_2/\text{N}_2/\text{Ar}$ chemistry.

Figure 15 presents the FESEM images of 250 nm diameter starting circle pattern etched using pure Cl_2 and pure Ar chemistry. For smaller diameter structures, mask erosion is more dominant. As seen in Sec. III A, etch using pure Cl_2 results in vertical sidewalls, with a small extent of mask erosion. It is clear comparing Figs. 3 and 5(a) that the ratio d_f/d_i (where d_f is the final tip diameter of the pillar and d_i is the initial etch mask diameter) is a function of the etch time t , and can be expressed as

$$\frac{d_f}{d_i} = \frac{d_i - \alpha t}{d_i}, \quad (5)$$

where α is the rate of lateral mask erosion. For $d_i \gg \alpha t$, i.e., for large diameter features, the ratio d_f/d_i approaches 1. For instance, for pure Cl_2 , for the 850 nm diameter etch mask the ratio d_f/d_i is 0.9, whereas for 250 nm diameter mask it is 0.6. If the parameter α is known for all etch chemistries and as a function of time, then we can produce features with any diameter, even with diameters smaller than the lithographic limit. Figure 15(b) shows that by changing the etch condition from a combination of chemical and physical, i.e., pure Cl_2 , to pure physical, i.e., pure Ar, significant tapering of the etch profiles can be obtained. Thus for pure argon, with 250 nm

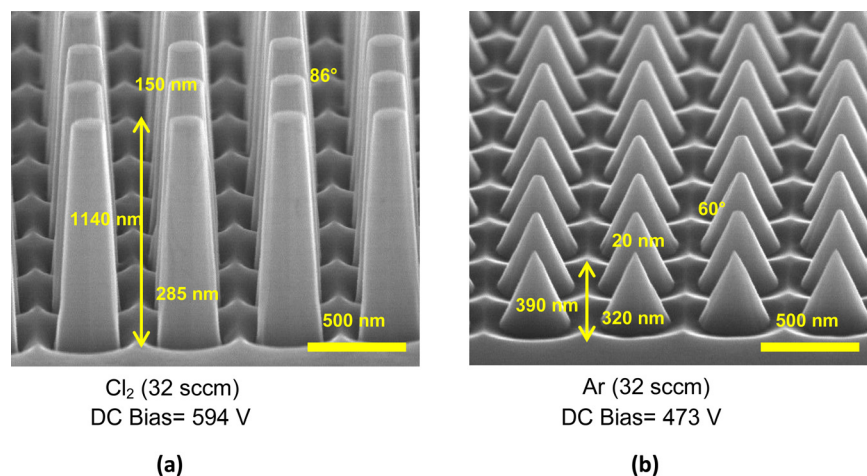


FIG. 15. (Color online) (a) FESEM image of GaN nanocolumns etched using pure Cl_2 (32 SCCM). (b) FESEM image of nanocones formed by etching GaN using pure Ar (32 SCCM). The starting etch pattern was 250 nm circle. Other etching parameters were ICP power 800 W, rf power 300 W, pressure 0.66 Pa, and substrate temperature 40 °C. The dc self-bias values are indicated at the bottom of the images.

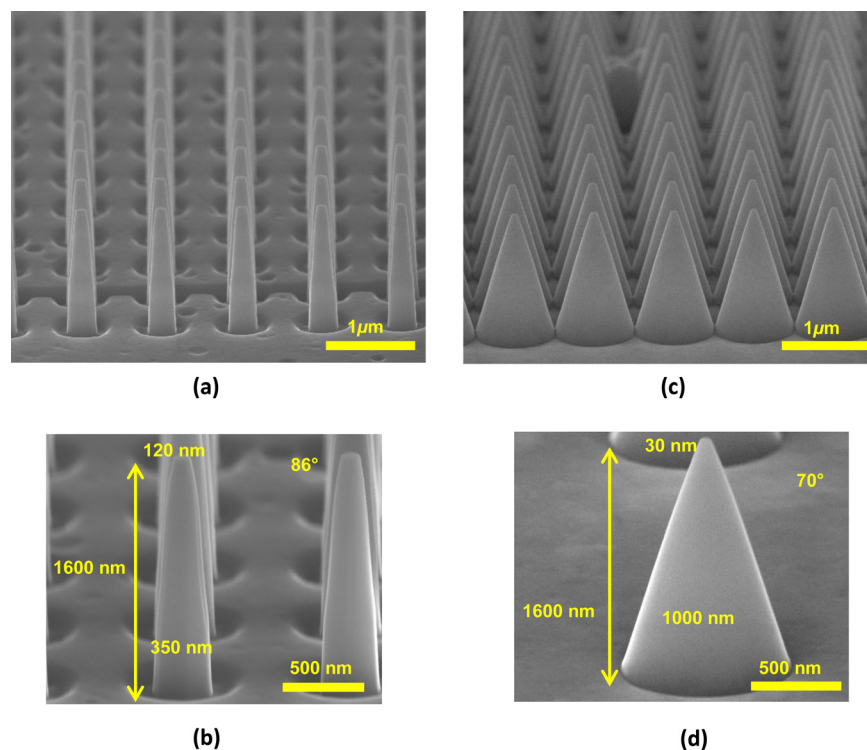


FIG. 16. (Color online) FESEM image of GaN etched at two different substrate temperatures using 250 nm diameter initial circular etch mask by $\text{Cl}_2/\text{N}_2/\text{Ar}$ (25/5/2 SCCM) chemistry. For all the images the etch conditions were ICP power 1500 W, rf power 300 W, pressure 0.66 Pa, and flow rate 32 SCCM. (a) Nanopillars etched at 40 °C, (b) high magnification image showing single nanocolumns, (c) FESEM image of nanocones formed by etching GaN at -120 °C, and (d) high magnification image of nanocone with tip diameter of 30 nm.

starting diameter of the etch mask, we are able to produce nanocones, with tip diameter around 20 nm.

From the temperature-dependent etching experiments presented in Sec. III F, it is indicative that the temperature is also another “design” parameter that can be varied to produce structures with various shapes. For most applications of nanoscale structures, high-aspect ratio is needed. For example, nanowires grown using chemical vapor deposition often have aspect ratios of 100 or higher. In order to develop high-aspect ratio structures using a top-down technique, we need high etch rate, anisotropic profile with smooth sidewalls. As seen from Sec. III C, high etch rates with smooth morphology can be obtained using high ICP power (1500 W). On the other hand, from Sec. III F we learned that by reducing the substrate temperature, we can produce angled sidewalls. In Figs. 16(a) and 16(b), we show etched structure for 250 nm starting diameter of the etch mask, etched using $\text{Cl}_2/\text{N}_2/\text{Ar}$ (25/5/2 SCCM) recipe at 40 °C at high ICP power (800 W). This resulted in high anisotropic etch rate, producing nanorods of GaN with aspect ratio of 13.

However, with the same recipe, reduction in the substrate temperature to -120 °C resulted in the dramatically different patterns seen in Figs. 16(c) and 16(d). Tall nanocones (length 1.6 μm) with tip diameter 30 nm are produced [see Fig. 16(d)].

The nanostructures shown in Figs. 15 and 16 demonstrate the strength of this technique, i.e., high degree of control over shape and geometry, precise location and orientation, and capability to produce nanostructures over large areas on

a wafer. Quantifying the effect of ion induced damage in such structures and their usefulness in device structures remains to be done.

IV. SUMMARY AND CONCLUSIONS

We have studied in detail the effects of various process parameters on GaN structure fabrication using Cl_2 -based chemistries. Special attention was given toward understanding dominant etch mechanisms in various regimes. The objective of this paper was to establish ICP etching as a top-down tool for fabrication of HAR GaN nanoscale structures. To that effect we have identified a set of parameters that allowed us to control the dimensions and shapes of the features.

In the future, we plan to utilize such large-area nanostructures for device applications. In order to realize high performance device, etched surfaces with minimal roughness and subsurface damage are essential. Although ICP etching produces less damage than RIE, subsurface damage might be present. We plan to utilize postetch chemical and thermal treatments for removal of the ion-damaged layer, and subsequently utilize these structures for device fabrication.

ACKNOWLEDGMENTS

The nanostructures were fabricated at the Nanofab clean room of the NIST Center for Nanoscale Science and Technology. The University of Maryland portion of the work was partially supported by the Defense Threat Reduction Agency, Basic Research Award No. HDTRA1-10-1-0107.

The authors thank Lei Chen of CNST (NIST) for his assistance with the ICP processing. Certain commercial equipment instruments or materials are identified in this paper to foster understanding. Such identification does not imply recommendation or endorsement by the National Institute of Standards and Technology nor does it imply that the materials or equipment identified are necessarily the best available for the purpose.

- ¹Fang Qian, Silvija Gradecak, Yat Li, Cheng-Yen Wen, and Charles M. Lieber, *Nano Lett.* **5**, 2287 (2005).
- ²Justin C. Johnson, Heon-Jin Choi, Kelly P. Knutsen, Richard D. Schaller, Peidong Yang, and Richard J. Saykally, *Nature Mater.* **1**, 106 (2002).
- ³P. T. Blanchard, K. A. Bertness, T. E. Harvey, L. M. Mansfield, A. W. Sanders, and N. A. Sanford, *IEEE Trans. Nanotechnol.* **7**, 760 (2008).
- ⁴G. S. Aluri, A. Motayed, A. V. Davydov, V. P. Oleshko, K. A. Bertness, N. A. Sanford, and M. V. Rao, *Nanotechnology* **22**, 295503 (2011).
- ⁵Stephen D. Hersee, Xinyu Sun, and Xin Wang, *Nano Lett.* **6**, 1808 (2006).
- ⁶Aric Sanders *et al.*, *Nanotechnology* **22**, 465703 (2011).
- ⁷Liq Iming *et al.*, *Opt. Express* **19**, 25528 (2011).
- ⁸P. D. Yang, R. X. Yan, and M. Fardy, *Nano Lett.* **10**, 1529 (2010).
- ⁹R. J. Shul *et al.*, *Appl. Phys. Lett.* **69**, 1119 (1996).
- ¹⁰S. A. Smith, C. A. Wolden, M. D. Bremser, A. D. Hanser, R. F. Davis, and W. V. Lampert, *Appl. Phys. Lett.* **71**, 3631 (1997).
- ¹¹R. J. Shul *et al.*, *J. Vac. Sci. Technol. A* **16**, 1621 (1998).
- ¹²J. K. Sheu, Y. K. Su, G. C. Chi, M. J. Jou, C. C. Liu, C. M. Chang, and W. C. Hung, *J. Appl. Phys.* **85**, 1970 (1999).
- ¹³H. S. Kim, G. Y. Yeom, J. W. Lee, and T. I. Kim, *J. Vac. Sci. Technol. A* **17**, 2214 (1999).
- ¹⁴Y. B. Hahn, D. C. Hays, S. M. Donovan, C. R. Abernathy, J. Han, R. J. Shul, H. Cho, K. B. Jung, and S. J. Pearton, *J. Vac. Sci. Technol. A* **17**, 768 (1999).
- ¹⁵Lee Ji-Myon, Chang Ki-Myung, Lee In-Hwan, and Park Seong-Ju, *J. Electrochem. Soc.* **147**, 1859 (2000).
- ¹⁶Emilie Despiau-Pujo, Pascal Chabert, Shailendra Bansropun, Didier The-not, Patrick Plouhinec, and Simone Cassette, *J. Vac. Sci. Technol. B* **28**, 693 (2010).
- ¹⁷Bifeng Rong, H. W. M. Salemink, E. M. Roeling, R. van der Heijden, F. Karouta, and E. van der Drift, *J. Vac. Sci. Technol. B* **25**, 2632 (2007).
- ¹⁸T. Stomeo *et al.*, *Proc. SPIE* **7713**, 771316 (2010).
- ¹⁹H. V. Jansen, M. J. de Boer, S. Unnikrishnan, M. C. Louwerse, and M. C. Elwenspoek, *J. Micromech. Microeng.* **19**, 033001 (2009).
- ²⁰M. J. Cooke and G. Hassall, *Plasma Sources Sci. Technol.* **11**, A74 (2002).
- ²¹F. A. Khan, L. Zhou, A. T. Ping, and I. Adesida, *J. Vac. Sci. Technol. B* **17**, 2750 (1999).
- ²²S. Tinck, W. Boullart, and A. Bogaerts, *J. Phys. D: Appl. Phys.* **41**, 065207 (2008).
- ²³J. D. Plummer, M. D. Deal, and P. B. Griffin, *Silicon VLSI Technology Fundamentals, Practice and Modeling* (Prentice Hall, Upper Saddle River, NJ, 2000).
- ²⁴G. S. Oehrlein, *Reactive Ion Etching: Handbook of Plasma Processing Technology*, edited by S. M. Rossmagel (Noyes, Park Ridge, NJ, 1990).
- ²⁵Y. H. Im, J. S. Park, Y. B. Hahn, K. S. Nahm, Y. S. Lee, B. C. Cho, K. Y. Lim, H. J. Lee, and S. J. Pearton, *J. Vac. Sci. Technol. A* **18**, 2169 (2000).
- ²⁶E. Zhirnov, S. Stepanov, A. Gott, W. N. Wang, Y. G. Shreter, D. V. Tar-khin, and N. I. Bochkareva, *J. Vac. Sci. Technol. A* **23**, 687 (2005).
- ²⁷J. Ladroue, A. Meritan, B. Boufnichel, P. Lefauchaux, P. Ranson, and R. Dussart, *J. Vac. Sci. Technol. A* **28**, 1226 (2010).
- ²⁸B. Rong, E. van der Drift, R. J. Reeves, W. G. Sloof, and R. Cheung, *J. Vac. Sci. Technol. B* **19**, 2917 (2001).